The Astrophysical Journal, 900:38 (11pp), 2020 September 1 https://doi.org/10.3847/1538-4357/aba52a

Electric Currents through J-shaped and Non-J-shaped Flare Ribbons

Yuwei He[1], Rui Liu[1,2,3], Lijuan Liu[2,4], Jun Chen[1], Wensi Wang[1], and Yuming Wang[1,2]
[1] CAS Key Laboratory of Geospace Environment, Department of Geophysics and Planetary Sciences, University of Science and Technology of China, Hefei, Anhui 230026, People's Republic of China; rliu@ustc.edu.cn
[2] CAS Center for Excellence in Comparative Planetology, Hefei, Anhui 230026, People's Republic of China
[3] Mengcheng National Geophysical Observatory, University of Science and Technology of China, Mengcheng, Anhui 233500, People's Republic of China
[4] School of Atmospheric Sciences, Sun Yat-sen University, Zhuhai, Guangdong 519082, People's Republic of China
Received 2020 June 28; revised 2020 July 8; accepted 2020 July 10; published 2020 August 28

Abstract

Increasing attention has recently been paid to solar flares exhibiting double-J-shaped ribbons in the lower solar atmosphere, in the context of extending the two-dimensional standard flare model to three dimensions, as motivated by the spatial correlation between photospheric current channels and flare ribbons. Here, we study the electric currents through the photospheric area swept by flare ribbons (termed the synthesized ribbon area (SRA)), with a sample of 71 two-ribbon flares, of which 36 are J-shaped. Electric currents flowing through one ribbon are highly correlated with those flowing through the other, and they therefore belong to the same current system. The nonneutrality factor of this current system is independent of the flare magnitude, implying that both direct and return currents participate in flares. J-shaped flares are distinct from non-J-shaped flares in the following ways: (1) electric-current densities within the J-shaped SRA are significantly smaller than those within the non-J-shaped SRA, but the J-shaped SRA and its associated magnetic flux is also significantly larger. (2) Electric currents through the SRA are positively correlated with the flare magnitude, but J-shaped flares show a stronger correlation than non-J-shaped flares. (3) The majority (75%) of J-shaped flares are eruptive, while the majority (86%) of non-J-shaped flares are confined; accordingly, hosting active regions of J-shaped flares are more likely to be sigmoidal than non-J-shaped flares. Thus, J-shaped flares constitute a distinct subset of two-ribbon flares, probably representative of eruptive ones. Further, we found that combining the SRA and its associated magnetic flux has the potential to differentiate eruptive from confined flares.

Unified Astronomy Thesaurus concepts: Solar flares (1496); Solar active regions (1974); Solar storm (1526); Solar coronal mass ejections (310); Magnetic fields (994)

1. Introduction

Solar flares are among the most energetic phenomena in our solar system. The flare emission spans the whole range of the electromagnetic spectrum, and is often associated with particle acceleration and coronal mass ejections. Understanding the physical mechanism of solar flares is not only important for forecasting the space weather at Earth, but also for understanding similar physical processes in stellar flares as well as on planetary magnetospheres (e.g., Zhong et al. 2020) and active galactic nuclei (e.g., Barret & Cappi 2019). Although the complexity and diversity of flare phenomena makes it impossible to build a "universal" flare model that is capable of explaining all observational aspects in all events, the standard or CSHKP flare model (Carmichael 1964; Sturrock 1966; Hirayama 1974; Kopp & Pneuman 1976) is successful in explaining the major characteristics of two-ribbon eruptive flares, and has formed the basis for our understanding of solar flares for decades (Priest & Forbes 2002).

Solar eruptive phenomena draw energy from coronal magnetic fields (Forbes 2000). The magnetic field $\boldsymbol{B}$ can always be decomposed into a current-free, potential component $\boldsymbol{B}_p$ and a current-carrying, nonpotential component $\boldsymbol{B}_c$, so that the magnetic energy E_m in a volume V can be written as (Sakurai 1981)

$$E_m = \int_V \frac{B^2}{8\pi}\, dV = \frac{1}{8\pi}\int_V B_p^2\, dV + \frac{1}{2c}\int_V \boldsymbol{A}_c \cdot \boldsymbol{J}\, dV, \quad (1)$$

where $\boldsymbol{B}_c = \nabla \times \boldsymbol{A}_c$ and $\boldsymbol{J} = \frac{c}{4\pi}\nabla \times \boldsymbol{B}_c$, as $\nabla \times \boldsymbol{B}_p = 0$. The first term is the energy of the potential field, which is produced by current sources located within the interior of the Sun. The energy powering solar eruptions can only be contained in the second term that is associated with electric currents in the solar corona. The most rapid release of this "free" magnetic energy is manifested as flares. Because of the huge magnetic Reynolds number in the corona, electric currents must be concentrated into small regions such as narrow current sheets, across which magnetic connectivity changes rapidly, generally known as quasi-separatrix layers (QSLs; Démoulin 2006). QSLs are preferential sites for magnetic reconnection, which drives the processes of plasma heating and particle acceleration in flares. Due to the requirement of electric-current continuity, concentrations of electric currents in the photosphere are believed to be the imprints of coronal current sheets (Fleishman & Pevtsov 2018). During the flare, the release of free magnetic energy stored in the corona can be attributed to a geometric reconfiguration of the current paths, with the magnitudes of currents at the footpoints of the current system being fixed to a large extent (Melrose 2017). During some flares, however, horizontal electric currents tend to concentrate at lower altitudes around the polarity-inversion line (PIL) than before the eruption (e.g., Liu et al. 2012, 2014; Sun et al. 2012), while vertical electric currents tend to increase in localized ribbons (e.g., Janvier et al. 2014, 2016; Sharykin et al. 2020).

From an observational perspective, only the vertical component of the electric-current density J_z can be derived from photospheric vector magnetograms, which are normally

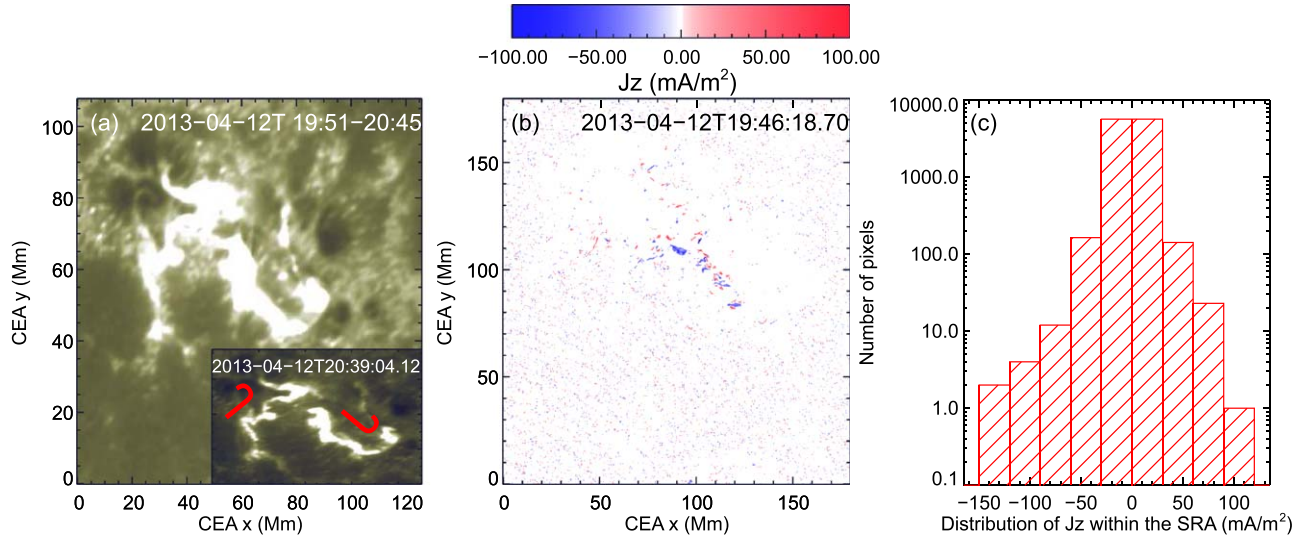

Figure 1. An exemplary J-shaped flare observed on 2013 April 12. (a) AIA 1600 Å emission averaged over from the flare onset to end time; the image is projected to CEA coordinates, and the inset shows flare ribbons at a time instance. The J shapes are illustrated by two reverse Js. (b) Distribution of preflare J_z in the same field of view as panel (a) at 19:46 UT, in which pixels with $|J_z|$ below 22 mA m^{-2} are assigned zero values, hence shown in white. (c) Histograms of J_z within the SRA, including $|J_z|$ values below 22 mA m^{-2}.

limited to a single height. With the measurements of photospheric transverse magnetic fields becoming more and more reliable, it has been well known that a close spatial relationship exists between the vertical electric currents at the photosphere and the deposition sites of flare energy at the chromosphere as represented by bright Hα kernels (e.g., Moreton & Severny 1968; Lin & Gaizauskas 1987; Romanov & Tsap 1990; de La Beaujardiere et al. 1993; Leka et al. 1993; Sharykin & Kosovichev 2014), UV/EUV emission (e.g., Janvier et al. 2014, 2016; Sharykin et al. 2020), or hard X-ray emission (e.g., Canfield et al. 1992; de La Beaujardiere et al. 1993; Li et al. 1997; Musset et al. 2015; Sharykin et al. 2020). However, these flare kernels are often not exactly cospatial with the locations of strongest electric-current densities, but adjacent to the current channels (e.g., Romanov & Tsap 1990; Canfield et al. 1992; de La Beaujardiere et al. 1993; Leka et al. 1993; Li et al. 1997), which might result from magnetic reconnection in a quadrupolar magnetic field (Aschwanden et al. 1999). Thus, the distribution of preflare electric-current densities in the photosphere provides important clues to the coronal currents accessible to flares.

More recently, aided by nonlinear force-free field or MHD modeling of the coronal magnetic field, it has been demonstrated that Hα and UV flare ribbons often coincide with the footprints of QSLs (e.g., Janvier et al. 2014, 2016; Liu et al. 2014, 2016, 2018; Jiang et al. 2018; Su et al. 2018). In particular, the footprints of the QSLs wrapping around a magnetic flux rope, the core structure of coronal mass ejections (Vourlidas et al. 2013; Georgoulis et al. 2019), correspond to a pair of J-shaped ribbons of high electric-current densities; the hooks of J-shaped ribbons outline the edge of the rope legs (Janvier et al. 2014, 2016; Wang et al. 2017). Motivated by these observational and modeling results, it has been proposed that the two-dimensional standard model can be extended to three dimensions to address the shape, location, and dynamics of flares with double-J-shaped ribbons (Aulanier et al. 2013, 2012; Janvier et al. 2013, 2015). However, not all two-ribbon flares are J-shaped; in fact, many typical two-ribbon flares (e.g., Figure 1 in Qiu et al. 2010) do not exhibit hooks at the ends of flare ribbons. Hence, it is unclear whether a canonical J-shaped flare, which breaks the translational symmetry along ribbons but introduces a twofold rotational symmetry (i.e., the ribbon morphology does not change by a rotation of 180°), can represent classic two-ribbon flares in the general 3D context.

In this paper, we tackle this question by investigating the distribution of pre-eruption photospheric electric currents associated with flare ribbons. Since the two ribbons often move away from each other during the impulsive phase of flares, we consider the photospheric electric currents through the total area swept by flare ribbons, termed the synthesized ribbon area (SRA) hereafter, instead of the area covered by flare ribbons at any time instance. We present the methods in Section 2, the statistical analysis in Section 3, and make concluding remarks in Section 4.

2. Data and Methods

2.1. Selection of Events

We selected two-ribbon flares of GOES-class M1.0 and above from the database provided by Kazachenko et al. (2017). The database covers all flare-ribbon events between 2010 April and 2016 April recorded by the Solar Dynamics Observatory (SDO; Pesnell et al. 2012), corresponding to GOES-class C1.0 and above within 45° from the central meridian. By visually examining flare ribbons observed by the ultraviolet 1600 Å passband of the Atmospheric Imaging Assembly (AIA; Lemen et al. 2012) on board SDO, we categorized the selected events into J-shaped flares (Figure 1(a)), if at least one of the two ribbons exhibits a hooked shape at the ribbon end, and non-J-shaped flares (Figure 2(a)), if neither ribbon has a pronounced hook. It is interesting that J-shaped flares do not necessarily occur in a sigmoidal active region (indicated by an asterisk in Tables 1 and 2) that exhibits an overall S shape with two opposing bundles of coronal loops; but non-J-shaped flares can sometimes be hosted by a sigmoidal active region. In addition, we excluded two types of events: (1) those with material ejection visible near flare ribbons in AIA 1600 Å images; and (2) those with complex or remote ribbons beyond two major

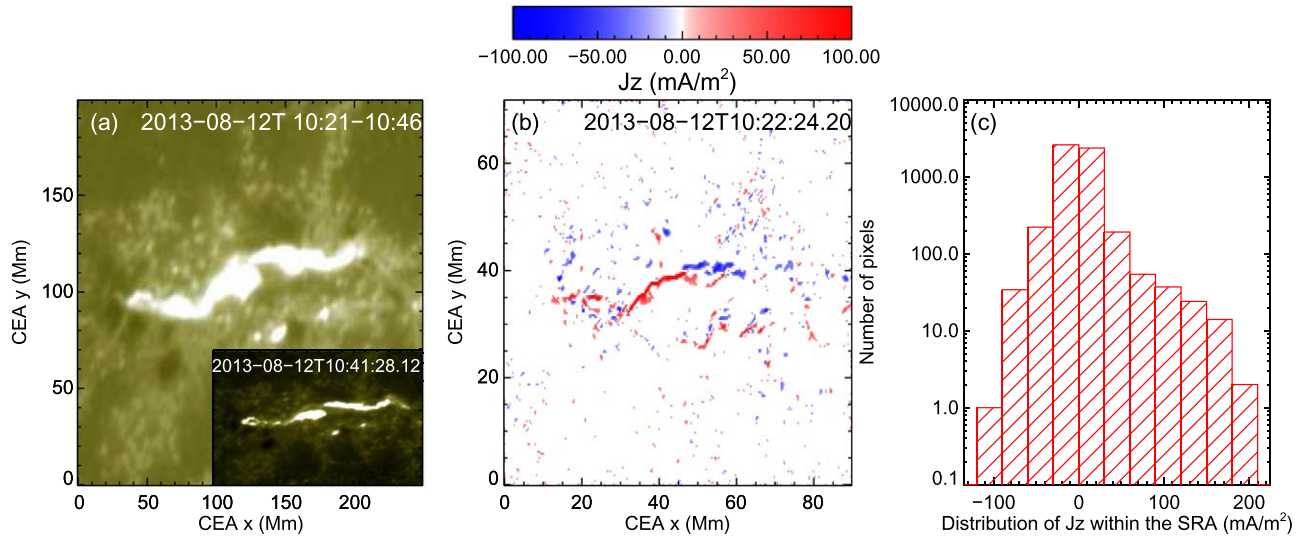

Figure 2. An exemplary non-J-shaped flare observed on 2013 August 12. (a) AIA 1600 Å emission averaged over from the flare onset to end time; the image is projected to CEA coordinates, and the inset shows flare ribbons at a time instance. (b) Distribution of preflare J_z in the same field of view as panel (a) at 10:22 UT, in which pixels with $|J_z|$ below 22 mA m^{-2} are assigned zero values, hence shown in white. (c) Histograms of J_z within the SRA, including $|J_z|$ values below 22 mA m^{-2}.

ribbons in AIA 1600 Å. Both scenarios could compromise a clear identification of the two major ribbons. In total, we have 36 J-shaped and 35 non-J-shaped flares.

2.2. Calculation of Electric-current Densities

We calculated the distribution of current density J_z in active regions of interest by Amepére's law,

$$\mu_0 J_z = \frac{\partial B_y}{\partial x} - \frac{\partial B_x}{\partial y}. \quad (2)$$

$B_{x,y}$ is obtained by the Helioseismic and Magnetic Imager (HMI; Scherrer et al. 2012) on board SDO. For each flare, we worked with a vector magnetogram taken immediately before the flare onset. These vector magnetograms are disambiguated and deprojected to the heliographic coordinates with a Lambert (cylindrical equal area; CEA) projection method, also known as the Space-Weather HMI Active Region Patches (SHARP) data. Computation of electric currents based on the above equation is subject to several uncertainties that are difficult to quantify, e.g., the 180° ambiguity in the horizontal field direction, and these uncertainties can be further amplified by partial derivatives. Considering the uncertainty in measuring the transverse component of photospheric magnetic field (∼100 G; Hoeksema et al. 2014) and SHARP's pixel size (0.36 Mm), we estimated that the uncertainty of J_z is about 22 mA m^{-2}. As a comparison, the average and standard deviation of $|J_z|$ in a box area in the quiet region is listed in the column "noise" in Tables 1 and 2, and the box typically occupies the lower-left corner (1/12 in length and 1/8 in width) of the SHARP map. One can see that in all cases the value of 22 mA m^{-2}, which significantly exceeds the average $|J_z|$ in the quiet region (∼10 mA m^{-2}), is a reliable representative of the noise level. Hence we considered only J_z above 22 mA m^{-2} in the statistical analysis below (Section 3). We have also carried out the same analysis without considering this threshold value, but got similar results and reached the same conclusions.

2.3. Identification of Flare Ribbons

We used AIA 1600 Å images to identify flare ribbons. The AIA 1600 Å passband provides full-disk images of the lower atmosphere at a temporal cadence of 24 s and a spatial resolution of 1.″2. To match the map of electric-current density with that of flare ribbons, we remapped 1600 Å images from the CCD coordinates to the CEA coordinates of the corresponding SHARP data. We detected flare ribbons by setting a threshold of about three to five times the average brightness of an AIA 1600 Å image immediately before the onset of each flare under investigation. We fine-tuned the exact threshold value case by case so that flare ribbons were visually captured as accurately as possible while as many as bright plages were excluded. This threshold value is varied by 15% to be taken as the upper and lower threshold. We flagged the pixels with brightness above the upper/lower threshold in each 1600 Å image, and collected all the flagged pixels during the interval from the GOES flare start to end time to construct "synthesized" flare ribbons. Meanwhile, we removed isolated pixels flagged outside the main ribbon area, and then constructed a binary mask for the synthesized flare ribbons by setting the flagged pixels to be unity and the rest to be zero. Applying the upper and lower threshold yields two slightly different ribbon masks and different ribbon areas. The average area is taken as the SRA. In the following, when calculating an electric-current parameter, we also apply the two ribbon masks that are associated with the upper and lower threshold, respectively, and then take the average to be the final result and half of the range to be the uncertainty.

2.4. Calculation of Electric-current Parameters

Multiplying the map of preflare J_z by the synthesized flare-ribbon mask, we obtained the distribution of J_z within the SRA (Figure 1(c) and 2(c)) as well as the mean ($\overline{|J_z|}$) and median ($\widetilde{|J_z|}$) of the absolute values of J_z. The direct current density $J_{\rm DC}$ is selected from J_z whose sign is consistent with the dominant current through the ribbon, as opposed to the return-current density $J_{\rm RC}$. Note that for simplicity, the signs of direct and return currents here are not defined according to the sign of

Table 1
Non-J-shaped Flares

No.	Flare SXR Peak Time	Position	NOAA AR	Category	$\overline{J_z^+}$ (mA m^{-2})	$\overline{J_z^-}$ (mA m^{-2})	$\widetilde{J_z^+}$ (mA m^{-2})	$\widetilde{J_z^-}$ (mA m^{-2})	I_{DC}^+ (A)	I_{RC}^+ (A)	I_{DC}^- (A)	I_{RC}^- (A)	Noise (mA m^{-2})
1	2011 Mar 9T14:02	N9W6	11166	C	28.98	30.03	25.84	26.76	3.10E+11	−1.59E+11	−4.13E+11	2.18E+11	6.67 ± 5.29
2	2011 Apr 22T04:57	S18E43	11195	C	27.25	26.45	25.06	24.68	2.99E+11	−1.68E+11	−4.04E+11	2.98E+11	7.33 ± 5.48
3	2011 Nov 6T06:35	N21E31	11339	C	40.02	35.04	30.42	29.68	−2.23E+12	1.61E+12	1.83E+12	−8.33E+11	7.87 ± 6.00
4	2011 Dec 26T02:27	S21W33	11387	E	36.96	35.01	32.33	29.37	−1.33E+12	7.42E+11	1.25E+12	−4.77E+11	10.12 ± 7.99
5	2011 Dec 31T16:26	S26E42	11389	C	35.29	40.32	29.53	30.80	−8.65E+11	6.69E+11	1.80E+12	−5.04E+11	8.44 ± 6.66
6	2012 Mar 6T00:28	N16E41	11429*	C	38.32	45.62	32.45	36.34	−1.70E+12	1.55E+12	4.61E+12	−1.47E+12	8.99 ± 6.97
7	2012 Mar 6T01:44	N17E41	11429*	C	41.11	44.64	34.29	34.23	−2.96E+12	1.69E+12	5.26E+12	−1.77E+12	9.15 ± 7.05
8	2012 Mar 6T22:53	N17E35	11429*	C	40.85	50.77	34.16	39.45	−3.68E+12	1.31E+12	6.65E+12	−1.58E+12	8.81 ± 6.74
9	2012 Mar 6T12:41	N18E36	11429*	C	34.96	46.73	30.29	37.24	−3.16E+12	1.51E+12	5.78E+12	−1.39E+12	10.54 ± 7.88
10	2012 Jun 6T20:06	S19W5	11494	E	30.80	33.40	27.45	28.30	−6.31E+11	5.56E+11	9.60E+11	−4.01E+11	9.05 ± 6.87
11	2012 Jun 13T13:17	S16E18	11504*	E	34.83	37.93	28.59	31.25	1.28E+12	−9.24E+11	−3.54E+12	1.72E+12	7.01 ± 5.54
12	2012 Jul 14T04:58	S22W30	11521	C	33.40	31.86	28.00	29.97	7.47E+11	−3.67E+11	−1.07E+12	2.50E+11	7.56 ± 5.98
13	2012 Nov 27T21:26	S14W41	11620	C	45.00	35.05	33.97	29.88	3.03E+12	−1.14E+12	−1.34E+12	8.72E+11	9.04 ± 7.07
14	2013 Aug 12T10:41	S17E19	11817*	E	36.53	50.98	31.57	37.60	−1.61E+12	3.51E+11	3.05E+12	−6.00E+11	9.71 ± 7.59
15	2013 Oct 22T00:22	N6E17	11875	C	37.33	35.00	31.24	30.13	1.26E+12	−1.24E+12	−1.03E+12	7.26E+11	9.67 ± 7.61
16	2013 Oct 24T00:08	N8W11	11875	C	39.12	40.47	32.38	31.89	2.58E+12	−1.73E+12	−3.00E+12	2.05E+12	8.56 ± 6.41
17	2013 Oct 24T10:09	N6W14	11875	C	36.56	40.75	31.68	31.37	1.93E+12	−1.27E+12	−2.34E+12	1.45E+12	6.13 ± 4.83
18	2013 Nov 16T04:53	S19W29	11900	C	39.82	46.78	32.97	34.14	−1.76E+12	1.78E+11	1.87E+12	−2.20E+11	7.80 ± 6.28
19	2014 Feb 1T01:25	S11E26	11967	C	33.61	54.77	28.59	40.56	−1.83E+12	7.78E+11	3.17E+12	−1.63E+12	7.07 ± 5.66
20	2014 Feb 2T22:04	S13E5	11967	C	41.83	42.75	35.92	34.25	−3.87E+12	1.69E+12	3.57E+12	−1.53E+12	7.64 ± 6.62
21	2014 Feb 4T01:23	S13W14	11967	C	48.31	61.78	38.07	44.68	−4.42E+12	8.43E+11	4.73E+12	−5.35E+11	9.49 ± 7.40
22	2014 Feb 4T09:49	S13W12	11967	C	50.76	54.57	40.46	40.12	−2.92E+12	8.55E+11	3.40E+12	−5.79E+11	8.70 ± 6.70
23	2014 Feb 11T16:51	S13E12	11974	E	36.11	38.15	31.12	30.31	2.31E+12	−1.38E+12	−2.30E+12	8.90E+11	7.65 ± 6.29
24	2014 Feb 13T08:12	S12W13	11974	C	46.40	41.96	34.43	33.43	3.31E+12	−2.71E+12	−2.66E+12	2.56E+12	9.04 ± 7.14
25	2014 Oct 20T09:11	S13E43	12192	C	39.38	44.86	32.87	33.12	−2.60E+12	1.88E+12	5.16E+12	−3.20E+12	8.33 ± 6.40
26	2014 Oct 20T20:04	S13E43	12192	C	31.65	36.85	28.04	32.86	−7.64E+11	6.68E+11	−6.55E+11	5.36E+11	8.32 ± 6.49
27	2014 Nov 7T10:22	N15E43	12205	C	46.59	37.01	36.24	30.78	2.50E+12	−7.27E+11	−1.50E+12	7.26E+11	11.14 ± 8.36
28	2014 Dec 1T06:41	S21E17	12222	C	28.58	29.31	27.19	26.59	−5.97E+11	2.68E+11	6.73E+11	−2.98E+11	10.23 ± 7.77
29	2014 Dec 4T18:25	S20W32	12222	C	36.07	33.92	29.82	28.11	3.12E+12	−3.08E+12	2.19E+12	−1.74E+12	9.68 ± 7.57
30	2014 Dec 4T19:41	S20W32	12222	C	32.81	25.76	30.01	24.70	−4.89E+11	1.54E+11	−1.79E+11	6.00E+10	8.46 ± 6.69
31	2014 Dec 5T12:25	S19W37	12222	C	31.72	29.36	27.67	26.11	1.21E+12	−8.91E+11	8.47E+11	−4.81E+11	9.03 ± 6.99
32	2014 Dec 19T09:44	S19W27	12242	C	29.66	28.30	27.58	25.75	5.17E+11	−3.67E+11	4.75E+11	−2.80E+11	7.85 ± 6.18
33	2014 Dec 21T07:32	S19W44	12242	C	38.49	34.61	32.19	29.55	2.21E+12	−1.10E+12	−1.29E+12	1.17E+12	8.10 ± 6.38
34	2015 Jan 26T16:53	S10E25	12268	C	37.74	39.66	30.47	32.43	−1.00E+12	5.68E+11	1.86E+12	−1.09E+12	9.62 ± 7.40
35	2015 Jun 20T06:48	N13E27	12371	C	42.39	44.21	30.17	33.78	−1.28E+12	2.86E+11	8.87E+11	−6.07E+11	10.73 ± 8.13

Note. "C" and "E" indicate confined and eruptive flares, respectively, in the "Category" column. Sigmoidal active regions are marked by asterisks.

Table 2
J-shaped Flares

No.	Flare SXR Peak Time	Position	NOAA AR	Category	$\overline{J_z^+}$ (mA m^{-2})	$\overline{J_z^-}$ (mA m^{-2})	$\widetilde{J_z^+}$ (mA m^{-2})	$\widetilde{J_z^-}$ (mA m^{-2})	I_{DC}^+ (A)	I_{RC}^+ (A)	I_{DC}^- (A)	I_{RC}^- (A)	Noise (mA m^{-2})
1	2010 Aug 7T18:24	N11E34	11093*	E	26.16	25.77	24.83	24.92	−6.74E+11	5.81E+11	6.05E+11	−4.20E+11	8.46 ± 6.46
2	2011 Jul 27T16:07	N20E37	11260	C	44.39	33.95	32.26	29.15	3.07E+12	−2.53E+12	2.39E+12	−1.63E+12	11.73 ± 8.64
3	2011 Aug 2T06:19	N16W8	11261	E	45.68	42.81	32.82	33.81	4.28E+12	−8.23E+11	−4.54E+12	1.94E+12	6.62 ± 5.50
4	2011 Aug 3T13:48	N16W30	11261	E	38.88	35.78	30.92	29.52	3.48E+12	−9.35E+11	−2.70E+12	1.23E+12	5.98 ± 4.62
5	2011 Nov 9T13:35	N25E34	11342	E	26.93	26.66	25.72	25.49	−5.50E+12	5.44E+12	−3.48E+12	3.14E+12	10.38 ± 7.74
6	2012 Mar 10T17:44	N18W18	11429	E	30.79	30.18	27.17	27.30	−3.06E+12	1.63E+12	3.87E+12	−1.86E+12	8.61 ± 6.74
7	2012 Mar 14T15:21	N14E5	11432	E	28.82	30.13	26.83	26.87	8.59E+11	−4.22E+11	−6.12E+11	4.76E+11	7.28 ± 5.78
8	2012 Apr 27T08:24	N11W30	11466*	C	27.90	29.52	25.89	26.53	−5.11E+11	4.04E+11	8.45E+11	−5.17E+11	9.22 ± 7.24
9	2012 Jul 10T05:14	S17E33	11520	C	34.37	49.04	29.38	41.64	9.58E+11	−3.38E+11	−2.33E+12	4.16E+11	7.23 ± 5.92
10	2012 Jul 10T06:27	S17E30	11520	C	34.11	39.05	30.13	34.74	1.00E+12	−4.01E+11	−1.57E+12	1.46E+11	8.77 ± 6.73
11	2013 Apr 11T07:16	N9E12	11719*	E	27.15	27.10	25.99	25.87	−2.60E+12	2.40E+12	1.02E+12	−9.50E+11	10.35 ± 7.73
12	2013 Apr 12T20:38	N22W42	11718	C	30.32	34.79	26.69	30.13	4.71E+11	−3.74E+11	−1.33E+12	1.11E+12	9.05 ± 7.43
13	2013 Aug 17T19:33	S7W29	11818*	E	39.30	29.16	31.43	26.34	1.66E+12	−6.56E+11	−1.61E+12	1.38E+12	10.27 ± 8.23
14	2013 Oct 13T00:43	S22E17	11865	E	38.67	34.96	29.42	31.25	2.11E+12	−3.79E+11	−1.78E+12	5.49E+11	10.03 ± 7.69
15	2013 Oct 15T08:38	S22W13	11865*	E	62.40	42.13	36.87	33.01	2.58E+12	−2.69E+11	−1.91E+12	2.92E+11	8.32 ± 6.40
16	2014 Jan 7T18:32	S14W7	11944	E	29.16	27.48	26.07	25.68	1.36E+12	−1.19E+12	−2.73E+12	2.51E+12	8.31 ± 6.53
17	2014 Jan 31T15:42	N9E36	11968	E	27.95	28.00	26.60	26.49	2.57E+12	−2.39E+12	−2.14E+12	1.90E+12	12.56 ± 9.45
18	2014 Feb 1T07:23	S11E23	11967	C	35.37	47.78	29.21	36.78	−1.50E+12	6.58E+11	3.67E+12	−1.43E+12	8.18 ± 7.08
19	2014 Mar 20T03:56	S14E35	12010	E	27.96	31.87	26.38	27.21	−4.49E+11	3.12E+11	−5.50E+11	3.94E+11	7.82 ± 6.27
20	2014 Jun 16T00:01	S22E7	12087	E	27.65	28.35	25.93	25.38	−4.70E+11	4.35E+11	−5.11E+11	4.37E+11	8.48 ± 6.69
21	2014 Aug 1T18:13	S9E12	12127	E	29.22	28.47	26.63	25.53	−1.02E+12	6.58E+11	7.45E+11	−4.24E+11	6.95 ± 5.37
22	2014 Aug 25T15:11	N5W36	12146	E	31.37	45.25	28.01	35.50	−1.46E+12	4.83E+11	2.07E+12	−5.76E+11	6.75 ± 5.35
23	2014 Aug 25T20:21	N9W38	12146	E	30.86	39.91	28.80	30.56	−1.81E+12	5.60E+11	2.27E+12	−3.58E+11	7.52 ± 6.02
24	2014 Sep 9T00:29	N12E29	12158*	E	34.83	34.11	30.14	29.05	−2.66E+12	1.50E+12	2.50E+12	−1.29E+12	8.63 ± 6.59
25	2014 Sep 28T02:58	S13W23	12173*	E	33.31	29.67	28.33	26.77	−1.58E+12	1.15E+12	9.70E+11	−4.65E+11	8.12 ± 6.23
26	2014 Oct 24T21:41	S16W21	12192*	C	33.19	30.54	27.29	26.88	−6.07E+12	4.73E+12	4.52E+12	−3.36E+12	8.21 ± 6.35
27	2014 Nov 7T17:26	N15E33	12205	E	46.31	35.80	30.97	29.95	7.78E+12	−1.60E+12	−5.02E+12	1.92E+12	8.19 ± 6.51
28	2014 Dec 17T19:01	S10E24	12241	C	37.50	37.16	30.06	31.31	1.26E+12	−2.71E+11	−1.66E+12	8.66E+11	9.81 ± 7.56
29	2014 Dec 18T21:58	S15E8	12241	E	37.02	36.65	31.02	32.10	3.35E+12	−5.08E+11	−4.39E+12	1.04E+12	9.69 ± 7.57
30	2014 Dec 21T12;17	S11W21	12241	E	32.45	27.36	26.76	25.72	6.35E+11	−2.60E+11	−5.53E+11	2.85E+11	8.16 ± 6.36
31	2015 Mar 12T12:14	S16E6	12297	C	35.59	41.53	29.54	28.62	9.92E+11	−2.77E+11	−1.07E+12	4.60E+11	7.54 ± 5.98
32	2015 Jun 21T02:36	N13E14	12371*	E	37.24	34.42	29.87	28.73	−1.70E+12	4.72E+11	1.36E+12	−9.95E+11	9.52 ± 7.25
33	2015 Jun 21T01:42	N12E13	12371*	E	38.77	33.72	29.92	30.27	−2.37E+12	7.99E+11	2.19E+12	−1.08E+12	8.21 ± 6.31
34	2015 Jun 22T18:23	N12W8	12371*	E	30.88	30.92	28.17	27.18	−3.01E+12	6.49E+11	2.97E+12	−1.22E+12	7.62 ± 6.02
35	2015 Nov 4T13:52	N6E3	12443	E	29.62	28.18	26.75	26.16	1.72E+12	−1.22E+12	−1.44E+12	1.43E+12	6.83 ± 5.56
36	2015 Nov 9T13:12	S11E41	12449*	E	27.87	28.42	26.24	26.44	−1.55E+12	1.48E+12	2.74E+12	−1.94E+12	9.81 ± 7.42

Note. "C" and "E" indicate confined and eruptive flares, respectively, in the "Category" column. Sigmoidal active regions are marked by asterisks.

magnetic helicity of the host active region as in MHD simulations (Schmieder & Aulanier 2018). In observations, it is more difficult to determine the sign of helicity than that of the dominant current. Summing up $J_{\rm DC}$ and $J_{\rm RC}$ on a flare ribbon, we obtained the direct current $I_{\rm DC}$ and return current $I_{\rm RC}$, respectively. The net current $I_{\rm net}$ is the algebraic sum of J_z over SRA, as opposed to the unsigned current $I_{\rm uns}$, which is the sum of $|J_z|$. The above quantities are listed in Tables 1 and 2. We adopted the superscript "+" or "−' to indicate that a parameter is given for a ribbon located on the positive or negative polarity side of the PIL. When the superscript is dropped, electric-current densities are sampled through both ribbons.

The above defined parameters of electric-current densities (Figure 3) and currents (Figure 4) flowing through the SRA of positive polarity are highly correlated with that of negative polarity. Hence it is reasonable to assume that they belong to the same current system, i.e., the electric currents flow out of one ribbon and into the other. Thus, following Georgoulis et al. (2012) we defined a nonneutrality factor $I_{\rm nn}$,

$$I_{\rm nn} = \frac{1}{2}\left(\frac{|I^{+}_{\rm net}|}{|I^{+}_{\rm DC}|} + \frac{|I^{-}_{\rm net}|}{|I^{-}_{\rm DC}|}\right), \tag{3}$$

so that $I_{\rm nn} = 0$ if electric currents through the SRA are balanced separately on either side of the PIL, i.e., neutralized, and that $I_{\rm nn} = 1$ if electric currents through the SRA are unneutralized. We noticed that Liu et al. (2017) used $|I_{\rm DC}/I_{\rm RC}|$ to measure the degree of current neutralization in active regions, but this parameter is less tractable than $I_{\rm nn}$ when $I_{\rm RC}$ is small.

3. Statistics

To evaluate whether J-shaped flares are distinct from non-J-shaped flares in terms of electric currents through SRA, we performed Welch's *t*-test to determine whether two samples of different sizes and variances belong to the same population, by comparing their sample means. The test defines a statistic t as follows,

$$t = \frac{\overline{X}_1 - \overline{X}_2}{\sqrt{\frac{s_1^2}{N_1} + \frac{s_2^2}{N_2}}}, \tag{4}$$

where $\overline{X}_1$, s_1^2, and N_1 are the first sample mean, sample variance, and sample size, respectively. The null hypothesis that two populations have equal means can be rejected if the resultant p-value is small enough. As a rule of thumb, one may deem that the two populations have significantly different means if $p \leqslant 0.01$, as there is less than a 1% probability that the null hypothesis is correct.

We found that the distributions of most current-density parameters are different for the two flare categories, which is manifested by the statistical significance in Welch's *t*-test. Specifically, both median and mean $|J_z|$ ($\widetilde{|J_z|}$ and $\overline{|J_z|}$, respectively) through J-shaped ribbons are smaller than those through non-J-shaped ribbons (Figures 5(a) and (b)). A similar result is found for the mean and median current densities for DC (Figures 5(c) and (d)) and RC (not shown). But we found no statistically significant differences between J-shaped and non-J-shaped flares in electric currents through the SRA, no matter if it is the direct, return, unsigned, or net current, or the dominance of direct current as measured by $I^{+}_{\rm DC}/I^{+}_{\rm RC}$ and $I^{-}_{\rm DC}/I^{-}_{\rm RC}$, or the current imbalance as measured by $I^{+}_{\rm DC}/I^{-}_{\rm DC}$ and $I^{+}_{\rm RC}/I^{-}_{\rm RC}$. Note that all the ratios are taken in their absolute values. However, J-shaped flares have a significantly larger SRA (Figure 5(e)) as well as larger unsigned magnetic flux through it $(|\Phi^{+}| + |\Phi^{-}|)/2$ (averaged over two ribbons; Figure 5(f)) than non-J-shaped flares.

We further examined the correlations between the flare magnitude as measured by the GOES class and the above parameters. None of the current-density parameters, $|J_z|$, $|J_{\rm RC}|$, or $|J_{\rm DC}|$ within the SRA, shows significant correlation with the flare magnitude. Averaged over two ribbons, the mean net current $(|I^{+}_{\rm net}| + |I^{-}_{\rm net}|)/2$, mean unsigned current $(|I^{+}_{\rm uns}| + |I^{-}_{\rm uns}|)/2$, and mean direct current $(|I^{+}_{\rm DC}| + |I^{-}_{\rm DC}|)/2$ are all positively correlated with the flare magnitude; but the correlation coefficient for J-shaped flares is consistently larger than non-J-shaped flare (Figures 6(a)–(c)). The flare magnitude is also positively correlated with both the SRA (Figure 6(e)) and magnetic flux through the SRA $(|\Phi^{+}| + |\Phi^{-}|)/2$ (Figure 6(f)), which is consistent with Kazachenko et al. (2017) and previous studies. On the other hand, it is surprising that the nonneutrality factor $I_{\rm nn}$ is almost independent of the flare magnitude (Figure 6(d)).

4. Discussion and Conclusion

To summarize, we confirmed that electric currents flowing through one ribbon are highly correlated with those through the other, and hence belong to the same current system pertinent to the two-ribbon flare. Importantly, we found that J-shaped flares are distinct from non-J-shaped flares in a few ways, as follows. First, $|J_z|$, $|J_{\rm DC}|$, and $|J_{\rm RC}|$ within the SRA of J-shaped flares are significantly smaller than those of non-J-shaped flares, but the SRA of J-shaped flares as well as the associated magnetic flux is significantly larger than that of non-J-shaped flares. In other words, smaller current densities in J-shaped flare ribbons are compensated for by a larger ribbon area, which explains why J-shaped flares are similar to non-J-shaped ones in terms of electric currents through the SRA. Second, the magnitudes of direct, net, and unsigned currents through the SRA are all positively correlated with the flare magnitude, but the correlation coefficient for J-shaped flares is generally larger than that for non-J-shaped flares. Third, the majority (27 of 36; 75%) of J-shaped flares are eruptive, while the majority (30 of 35; 86%) of non-J-shaped flares are confined; among the 28 hosting active regions for the J-shaped flares, 12 are sigmoidal regions,[5] yet among the 21 hosting active regions for the non-J-shaped flares, only three are sigmoidal. These differences highlight J-shaped flares as a distinct subset of two-ribbon flares, probably the representative of eruptive ones. These differences also imply a different magnetic configuration in J-shaped compared to non-J-shaped flares, which will be further explored in future work and should be taken into account in developing a three-dimensional model for two-ribbon flares as a whole.

Furthermore, the flare magnitude is independent of the nonneutrality factor $I_{\rm nn}$. In other words, it does not matter whether the electric currents flowing through flare ribbons are neutralized ($I_{\rm nn} = 0$), i.e., balanced separately on each ribbon, or, unneutralized ($I_{\rm nn} = 1$), i.e., the return current is negligible relative to the direct current through each ribbon. This may

[5] A special case is AR 11865, which is not yet sigmoidal at the time of Event #14 of a J-shaped flare, but becomes sigmoidal at the time of Event #15.

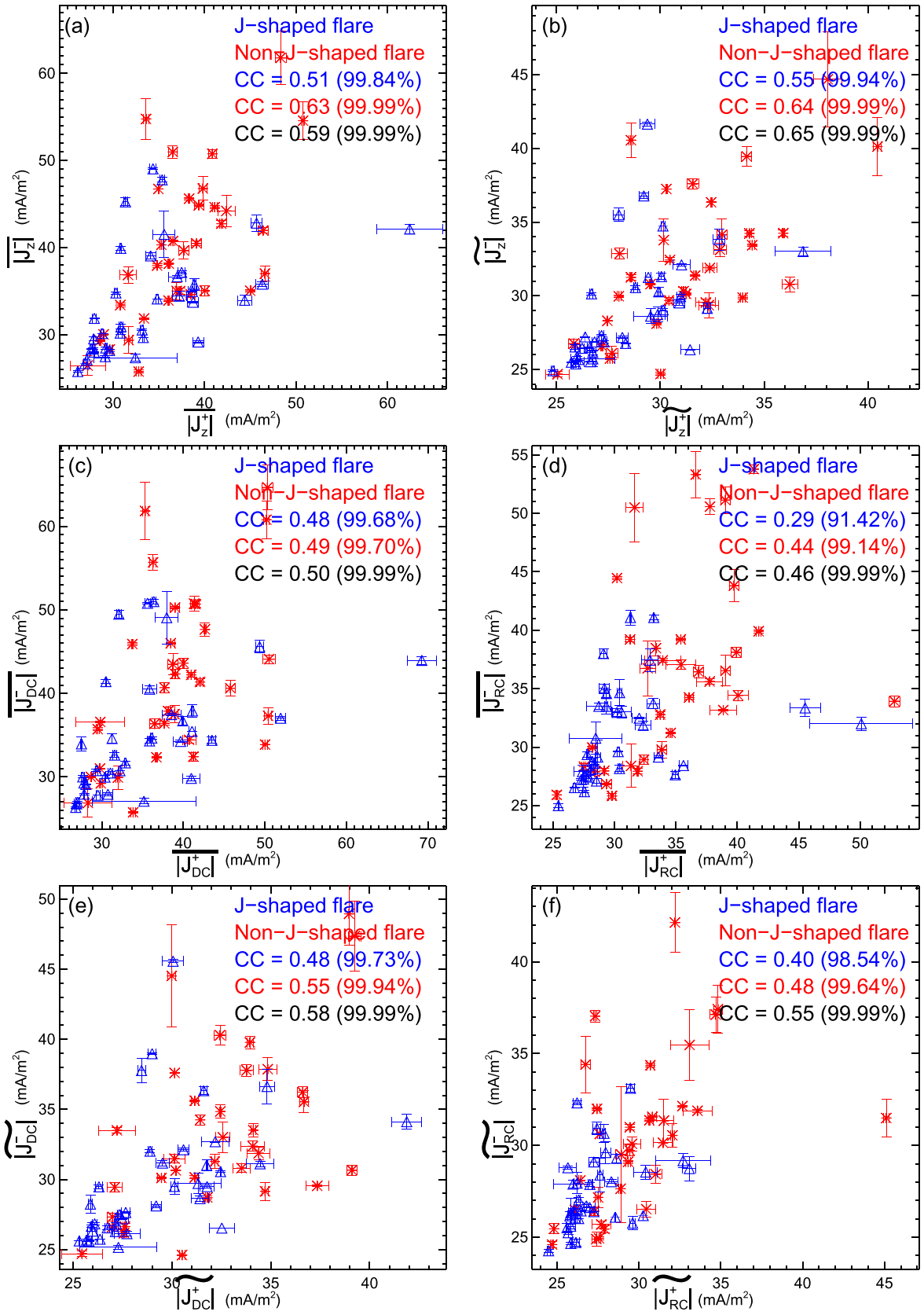

Figure 3. Electric-current densities within the synthesized ribbon of positive polarity vs. negative polarity. Red asterisks and blue triangles represent non-J-shaped and J-shaped flares, respectively. Annotated in each panel are the Pearson correlation coefficient (CC) and corresponding confidence level (in brackets) for each category (color coded) and the whole sample (black).

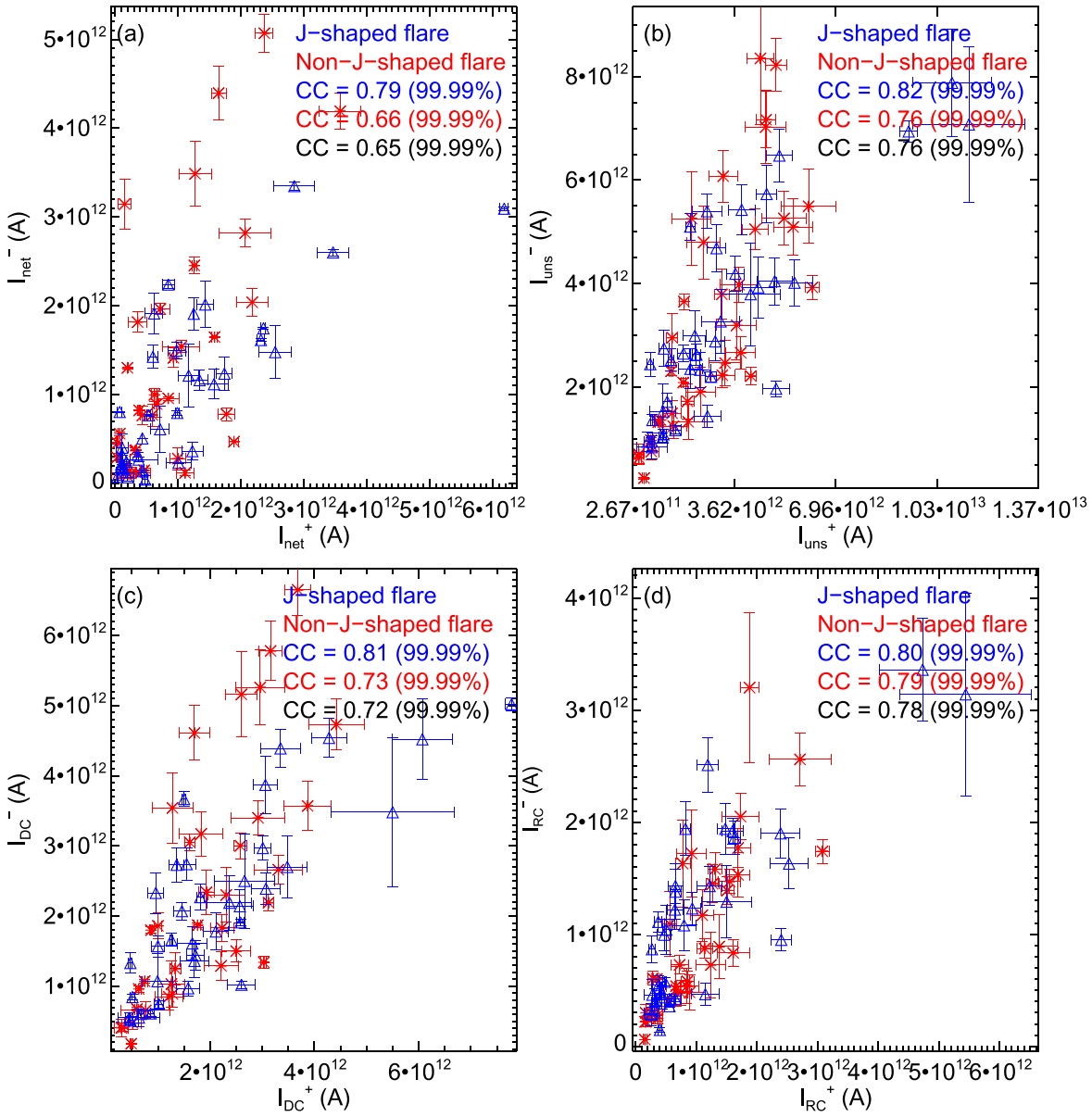

Figure 4. Electric currents through the synthesized ribbon of positive polarity vs. negative polarity. Red asterisks and blue triangles represent non-J-shaped and J-shaped flares, respectively. Annotated in each panel are the Pearson correlation coefficient (CC) and corresponding confidence level (in brackets) for each category (color coded) and the whole sample (black).

imply that both the direct and return current are involved in flares. With a weak positive correlation, a stronger direct current is associated with I_{nn} being closer to unity (left panel of Figure 7), but neither direct current nor I_{nn} is able to differentiate eruptive from confined flares. We further checked other parameters and any two of their combinations. The only pair that stands out is the SRA and the associated magnetic flux (right panel of Figure 7). Most of the flares are eruptive, if SRA exceeds 10^{15} m^2 and the average unsigned magnetic flux through each ribbon exceeds 4×10^{21} Mx. In contrast, if both parameters are below the above-mentioned threshold values, most of the flares are confined.

Using $|I_{DC}/I_{RC}|$ to measure the degree of current neutralization, Liu et al. (2017) found in a sample of four active regions that the two CME-producing regions are strongly nonneutralized ($|I_{DC}/I_{RC}| \approx 2$); the other two regions that did not produce CMEs are almost perfectly neutralized, but can still produce strong flares. They hence speculated that the presence or absence of a double-J pattern of direct currents around the PIL may indicate whether or not an active region will produce CMEs. More recent studies on larger samples found that CME/flare-productive active regions are more likely to be nonneutralized than quiet regions (Vemareddy 2019; Avallone & Sun 2020). Instead of examining the whole active region, our statistical study focuses on electric currents flowing though flare ribbons, in other words, the currents accessible to flares. This study shows that I_{nn} is similar to $|I_{DC}/I_{RC}|$ in its poor correlation with the flare magnitude, consistent with Liu et al. (2017), and that J-shaped flares are more likely to be eruptive than non-J-shaped ones. Moreover, we found that combining the ribbon area and its associated magnetic flux has the potential to differentiate eruptive from confined flares. Further study is needed to clarify the connection between electric currents in an active region and its productivity of flares and CMEs.

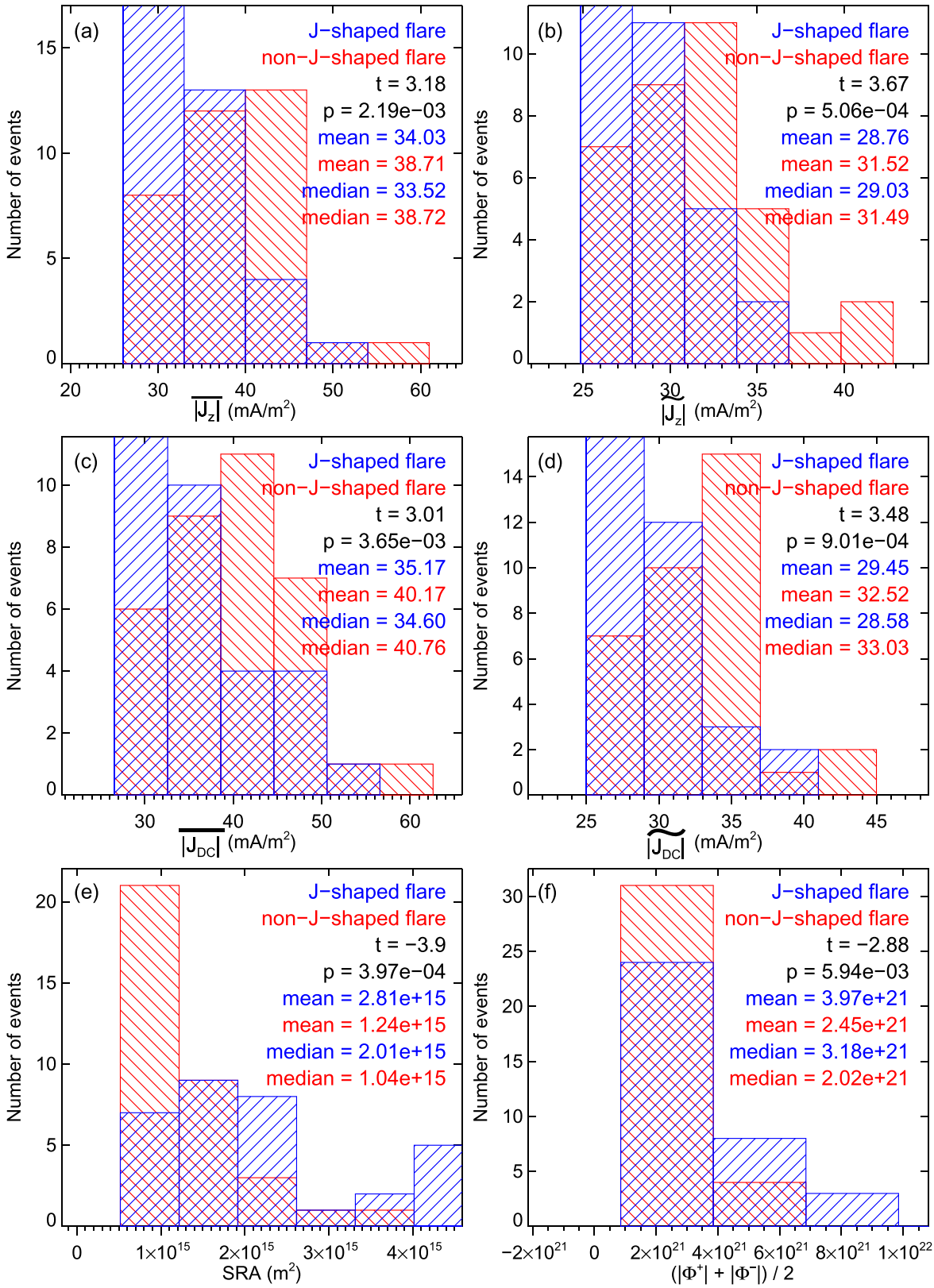

Figure 5. Histograms of parameters that display statistically significant differences between J-shaped and non-J-shaped flares. (a), (b) The mean and median of $|J_z|$ within the SRA, respectively; (c), (d) the mean and median of $|J_{DC}|$ within the SRA, respectively; (e) the distribution of the SRA; (f) the distribution of unsigned magnetic flux through the SRA, averaged over two ribbons. J-shaped (non-J-shaped) flares are indicated by blue (red) colors. Welch's statistic t and the corresponding p-value are annotated in each panel.

The authors thank the SDO Consortium for the excellent data. This work was supported by NSFC (grant Nos. 41761134088, 41774150, and 11925302), CAS Key Research Program (grant No. KZZD-EW-01-4), the fundamental research funds for the central universities, and the Strategic Priority Program of the Chinese Academy of Sciences (grant No. XDB41000000).

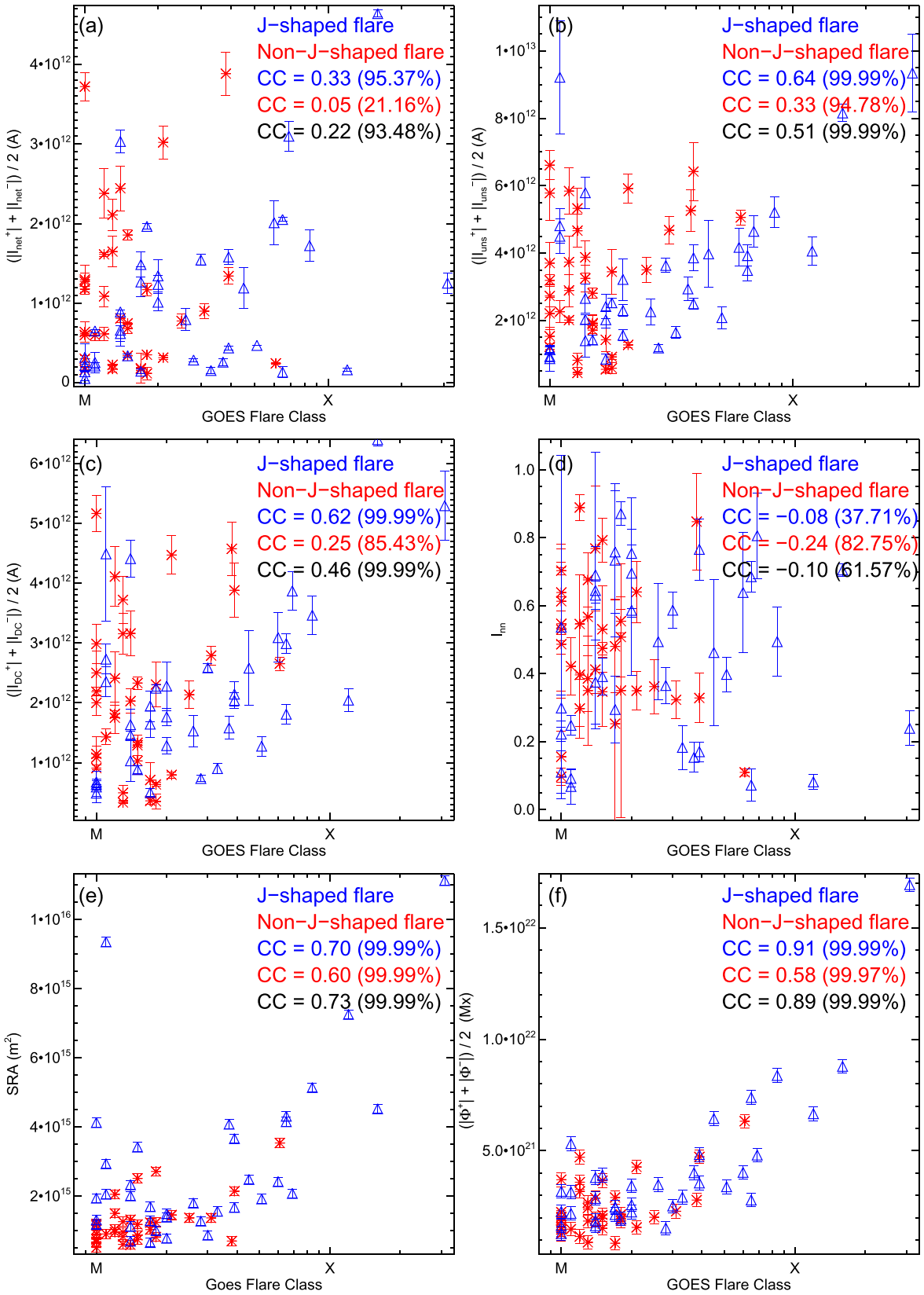

Figure 6. Electric currents and magnetic flux through the SRA in relation to GOES flare class. Plotted are (a) net current averaged over two ribbons, (b) unsigned current averaged over two ribbons, (c) direct current averaged over two ribbons, (d) nonneutrality factor as defined by Equation (3), (e) the SRA, and (f) magnetic flux through the SRA averaged over two ribbons. Red asterisks and blue triangles represent non-J-shaped and J-shaped flares, respectively. Annotated in each panel are the Pearson correlation coefficient (CC) and corresponding confidence level (in brackets) for each category (color coded) and the whole sample (black).

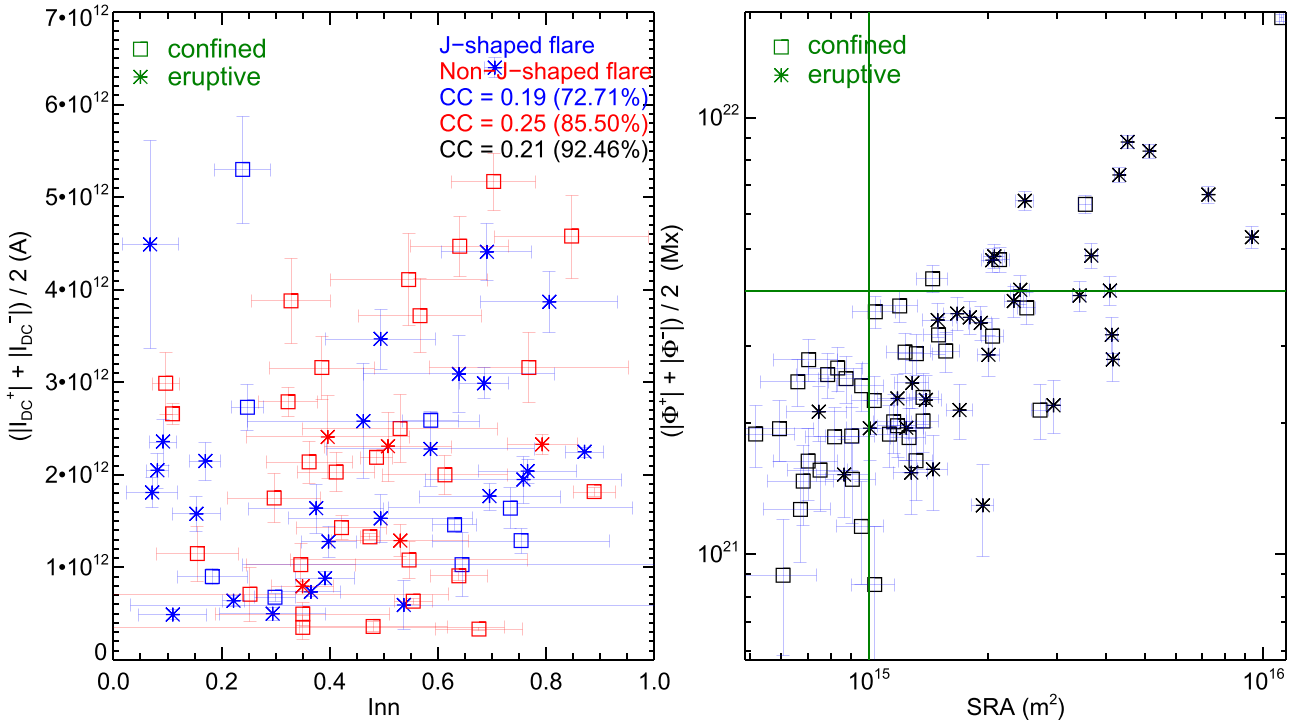

Figure 7. Eruptive and confined flares in different parameter spaces. Eruptive flares are marked by asterisks, and confined flares by squares. Left: nonneutrality factor vs. direct current. Right: SRA vs. its associated magnetic flux.

ORCID iDs

Rui Liu https://orcid.org/0000-0003-4618-4979
Lijuan Liu https://orcid.org/0000-0001-6804-848X
Jun Chen https://orcid.org/0000-0003-3060-0480
Wensi Wang https://orcid.org/0000-0002-9865-5245
Yuming Wang https://orcid.org/0000-0002-8887-3919

References

Aschwanden, M. J., Kosugi, T., Hanaoka, Y., Nishio, M., & Melrose, D. B. 1999, ApJ, 526, 1026
Aulanier, G., Démoulin, P., Schrijver, C. J., et al. 2013, A&A, 549, A66
Aulanier, G., Janvier, M., & Schmieder, B. 2012, A&A, 543, A110
Avallone, E. A., & Sun, X. 2020, ApJ, 893, 123
Barret, D., & Cappi, M. 2019, A&A, 628, A5
Canfield, R. C., Hudson, H. S., Leka, K. D., et al. 1992, PASJ, 44, L111
Carmichael, H. 1964, NASSP, 50, 451
de La Beaujardiere, J. F., Canfield, R. C., & Leka, K. D. 1993, ApJ, 411, 378
Démoulin, P. 2006, AdSpR, 37, 1269
Fleishman, G. D., & Pevtsov, A. A. 2018, in Electric Currents in Geospace and Beyond, ed. A. Keiling, O. Marghitu, & M. Wheatland (Washington, DC: American Geophysical Union), 43
Forbes, T. G. 2000, JGR, 105, 23153
Georgoulis, M. K., Nindos, A., & Zhang, H. 2019, RSPTA, 377, 20180094
Georgoulis, M. K., Titov, V. S., & Mikić, Z. 2012, ApJ, 761, 61
Hirayama, T. 1974, SoPh, 34, 323
Hoeksema, J. T., Liu, Y., Hayashi, K., et al. 2014, SoPh, 289, 3483
Janvier, M., Aulanier, G., Bommier, V., et al. 2014, ApJ, 788, 60
Janvier, M., Aulanier, G., & Démoulin, P. 2015, SoPh, 290, 3425
Janvier, M., Aulanier, G., Pariat, E., & Démoulin, P. 2013, A&A, 555, A77
Janvier, M., Savcheva, A., Pariat, E., et al. 2016, A&A, 591, A141
Jiang, C., Zou, P., Feng, X., et al. 2018, ApJ, 869, 13
Kazachenko, M. D., Lynch, B. J., Welsch, B. T., & Sun, X. 2017, ApJ, 845, 49
Kopp, R. A., & Pneuman, G. W. 1976, SoPh, 50, 85
Leka, K. D., Canfield, R. C., McClymont, A. N., et al. 1993, ApJ, 411, 370
Lemen, J. R., Title, A. M., Akin, D. J., et al. 2012, SoPh, 275, 17
Li, J., Metcalf, T. R., Canfield, R. C., Wülser, J.-P., & Kosugi, T. 1997, ApJ, 482, 490
Lin, Y., & Gaizauskas, V. 1987, SoPh, 109, 81
Liu, C., Deng, N., Liu, R., et al. 2012, ApJL, 745, L4
Liu, R., Chen, J., & Wang, Y. 2018, SCPMA, 61, 69611
Liu, R., Chen, J., Wang, Y., & Liu, K. 2016, NatSR, 6, 34021
Liu, R., Titov, V. S., Gou, T., et al. 2014, ApJ, 790, 8
Liu, Y., Sun, X., Török, T., Titov, V. S., & Leake, J. E. 2017, ApJL, 846, L6
Melrose, D. B. 2017, JGRA, 122, 7963
Moreton, G. E., & Severny, A. B. 1968, SoPh, 3, 282
Musset, S., Vilmer, N., & Bommier, V. 2015, A&A, 580, A106
Pesnell, W. D., Thompson, B. J., & Chamberlin, P. C. 2012, SoPh, 275, 3
Priest, E. R., & Forbes, T. G. 2002, A&ARv, 10, 313
Qiu, J., Liu, W., Hill, N., & Kazachenko, M. 2010, ApJ, 725, 319
Romanov, V. A., & Tsap, T. T. 1990, SvA, 34, 656
Sakurai, T. 1981, SoPh, 69, 343
Scherrer, P. H., Schou, J., Bush, R. I., et al. 2012, SoPh, 275, 207
Schmieder, B., & Aulanier, G. 2018, in Electric Currents in Geospace and Beyond, ed. A. Keiling, O. Marghitu, & M. Wheatland (Washington, DC: American Geophysical Union), 391
Sharykin, I. N., & Kosovichev, A. G. 2014, ApJL, 788, L18
Sharykin, I. N., Zimovets, I. V., & Myshyakov, I. I. 2020, ApJ, 893, 159
Sturrock, P. A. 1966, Natur, 211, 695
Su, Y., Liu, R., Li, S., et al. 2018, ApJ, 855, 77
Sun, X., Hoeksema, J. T., Liu, Y., et al. 2012, ApJ, 748, 77
Vemareddy, P. 2019, MNRAS, 486, 4936
Vourlidas, A., Lynch, B. J., Howard, R. A., & Li, Y. 2013, SoPh, 284, 179
Wang, W., Liu, R., Wang, Y., et al. 2017, NatCo, 8, 1330
Zhong, J., Wei, Y., Lee, L. C., et al. 2020, ApJL, 893, L18